

# Tuning Excitonic Properties of Pure and Mixed Halide Perovskite Thin Films via Interfacial Engineering

Katerina Nikolaidou, Som Sarang, Denzal Martin, Vincent Tung, Jennifer Q. Lu, and Sayantani Ghosh\*

The authors explore the potential of ZnO layers of different morphologies, including single crystalline, micro-structured, and nano-structured substrates, for tuning exciton binding energy and influencing charge extraction when interfaced with pure (CH<sub>3</sub>NH<sub>3</sub>PbI<sub>3</sub>) and mixed (CH<sub>3</sub>NH<sub>3</sub>PbI<sub>3-x</sub>Cl<sub>x</sub>) halide hybrid perovskite (PVSK) thin films. Electron microscopy characterization of the PVSK/ZnO interfaces are correlated with charge transfer properties, probed by means of temperature, power, and time-resolved photoluminescence (PL) spectroscopy. The results show that at room temperature, the single crystalline ZnO film promotes PL quenching, and reduces recombination lifetime along with exciton density in the PVSK films, all indicative of efficient electron extraction. Nevertheless, the micro-structured ZnO layers exhibit a mild increase of the PVSK PL at room temperature, and the nano-structured ZnO enhances PL by up to several thousand-fold, while simultaneously enhancing recombination rates by 50%. These trends are temperature dependent, and the findings highlight two opposing aspects of how excitonic dissociation in PVSK thin films is affected by the morphology of the underlying ZnO layers. While the single crystalline ZnO can be leveraged as an efficient electron extraction layer for application in photovoltaic devices, the micro- and nano-structured ones offer potential new opportunities for utilization of high quantum yield hybrid perovskites in opto-electronic platforms.

exceeding 20%<sup>[2–4]</sup> in perovskite (PVSK)-based photovoltaics. These superlative metrics can be attributed to the favorable characteristics of hybrid PVSKs as light harvesting media, including broadband absorption, high electron and hole mobilities, when compared to typical values in organic semiconductors, and long charge carrier lifetimes.<sup>[5,6]</sup> Furthermore, PVSKs can be prepared using solution-based, low-temperature techniques that allow for considerable flexibility.<sup>[7–10]</sup>

The characteristics that have brought cost-effective and high-efficiency solar cells closer to reality also lend themselves to a variety of other applications, such as in tunable lasers, light-emitting diodes, and photodetectors.<sup>[8,11,12]</sup> In all of these, efficient performance is strongly dependent on the optimal interaction at the interfaces between the active PVSK film and the extraneous layers implemented for charge dissociation, extraction, and conveyance. The properties of the electron and hole transport layers (ETL and HTL, respectively) therefore play critical roles in the device design.<sup>[13]</sup> Various

ETL materials have been incorporated in PVSK solar cells,<sup>[13–20]</sup> and among these, ZnO has proven superior in several respects as an ETL. For example, its electron mobility is in the range of 200–300 cm<sup>2</sup> V<sup>-1</sup> s<sup>-1</sup>, significantly higher than that of TiO<sub>2</sub>,<sup>[13]</sup> and additionally, there have been indications of its contribution to improving long-term operational stability<sup>[20]</sup> of PVSK devices. Aside from thin films and epi-layers, metal oxide nanostructures have also been incorporated as ETLs in solar cells as a means of increasing absorption cross section without adding to the physical size of the device. Nanowires and nanorods of TiO<sub>2</sub>, Y:TiO<sub>2</sub>, ZnO, and WO<sub>3</sub><sup>[18,21,22]</sup> have been implemented in PVSK solar cells as ETLs with promising results, and again, ZnO is an attractive candidate here too, as ZnO nanostructures can be grown at relatively low temperatures.<sup>[18,23,24]</sup>

Thus far, the research effort on investigating heterostructures comprising PVSK films and ZnO layers has been focused primarily on photovoltaic characterization. This has necessarily limited the perspective to optimization of power conversion efficiency alone, without systematically studying the fundamental processes occurring at the interface. A detailed and thorough understanding of the interaction between the two

## 1. Introduction

Hybrid organic–inorganic halide perovskites were first incorporated in solar cells in 2009 as sensitizers, with TiO<sub>2</sub> serving as the electron transport material, and resulted in a device with power conversion efficiency of 3.8%.<sup>[1]</sup> Since then, focused effort on device design and materials engineering have resulted in significant improvements, with power conversion efficiencies

K. Nikolaidou, S. Sarang, D. Martin, Prof. S. Ghosh  
School of Natural Sciences  
University of California  
Merced, CA 95344, USA  
E-mail: sghosh@ucmerced.edu

Prof. V. Tung, Prof. J. Q. Lu  
School of Engineering  
University of California  
Merced, CA 95344, USA

 The ORCID identification number(s) for the author(s) of this article can be found under <https://doi.org/10.1002/admi.201800209>.

DOI: 10.1002/admi.201800209

materials is necessary not just to optimize device design, but to allow correlation of ZnO layer morphology with charge extraction properties. Only then will it be possible to fully exploit the potential of hybrid perovskites for applications beyond photovoltaics. In this work, we quantify the interfacial interactions using recombination lifetime in PVSK as deposited on ZnO, as well as steady-state photoluminescence (PL) spectroscopy with varying temperature and excitation power.<sup>[21,25,26]</sup> The results obtained indicate that while single-crystalline ZnO can be leveraged as an efficient electron extraction layer for application in photovoltaic devices, the micro- and nanostructured layers lead to PVSK emission enhancement, the latter by almost a thousand-fold. While this is far from ideal for charge extraction, it opens new opportunities for other optoelectronic applications that can benefit by leveraging the high optical quantum yield of PVSK materials.

## 2. Results

### 2.1. ZnO Layer Characteristics

Figure 1 introduces the different ZnO substrates used in this study. The microstructured ZnO sample (MS-ZnO), shown in Figure 1a, consists of relatively large features, with lengths of  $\approx 1 \mu\text{m}$  and diameters ranging between 200 and 400 nm. The nanostructured ZnO sample (NS-ZnO) consists of nanowires that are  $\approx 1.5 \mu\text{m}$  long and 50 nm in diameter, shown in Figure 1b. The third ZnO layer used is a commercially acquired

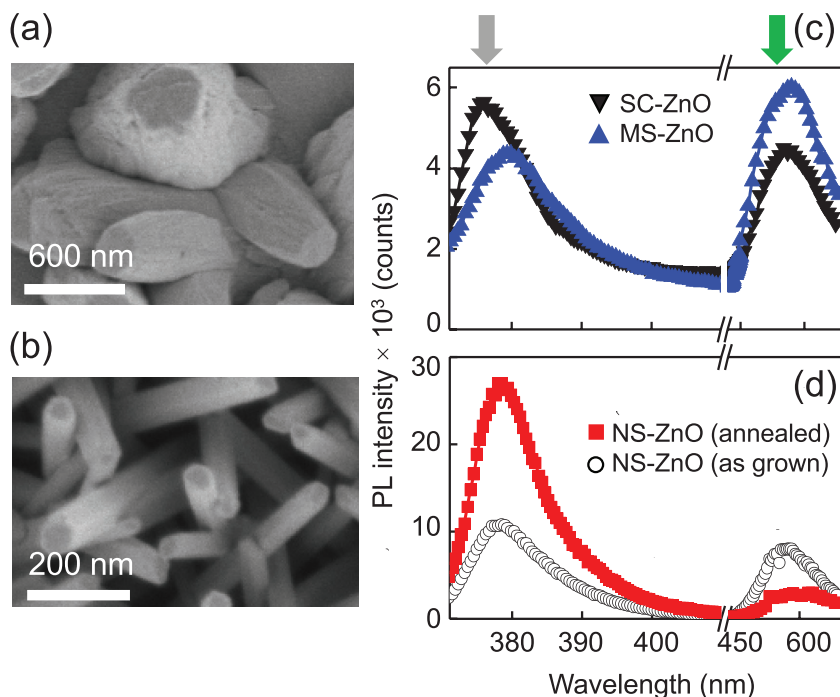


**Figure 1.** a,b) SEM image of microstructured (MS-ZnO) and nanostructured (NS-ZnO) layers. c) PL results comparing the emission from both the band edge (gray arrow) and defect states (green arrow) from single-crystalline (SC-ZnO) and microstructured (MS-ZnO) layers. d) PL of NS-ZnO layers pre- and post-annealing in air demonstrates significant success in suppressing defect emission and consequently, enhancing bandgap signal.

single crystal (SC-ZnO) from Tokyo Denpa Inc. The PL spectra of the three layers are summarized in Figure 1c,d. Figure 1c compares the PL of MS-ZnO and SC-ZnO. The emission centered around 380 nm is the direct bandgap emission, while the luminescence in the range 500–600 nm, routinely observed in ZnO samples, is associated with defects arising from surface states and oxygen vacancies.<sup>[27]</sup> The emission spectra of the NS-ZnO before and after annealing in Figure 1d show that these have the most intense PL, as the radial confinement of excitons within the nanostructures increase the probability of recombination.<sup>[28]</sup> Emission intensity of NS-ZnO is enhanced, and the defect emission significantly quenched, after annealing, a common observation attributed to improved crystallinity.<sup>[29,30]</sup> The emission peaks of the ZnO structures prepared in our laboratory are redshifted compared to the single-crystal emission, resultant of increased contribution from recombination of bound excitons as the size of the structure is reduced and carriers confined.<sup>[29,30]</sup>

### 2.2. PVSK Thin Film and ZnO Layer Interface Characteristics

Figure 2 is a compilation of morphological and fluorescence characteristics of the surface of the  $\text{CH}_3\text{NH}_3\text{PbI}_3$ -ZnO samples. Figure 2a is the scanning electron microscope (SEM) image of a PVSK film deposited on indium tin oxide (ITO) coated glass (ITO/PVSK), and shows uniform small grains, as is associated with PVSK thin films prepared with precursor containing lead acetate.<sup>[31]</sup> The choice of ITO-coated glass as the control sample

is motivated by the fact that along with FTO, ITO is one of the most commonly used substrates for PVSK thin film deposition. Given that ITO itself may act as an electron extraction layer, we have investigated PVSK deposited on glass without ITO coating to provide a second baseline. SEM imaging (Figure S1a,b, Supporting Information) and spectroscopy (Figure S1c,d, Supporting Information) data demonstrate that there is no noticeable difference between these two substrates, and therefore, ITO itself does not have a significant impact as an extraction layer. Figure 2b shows the PVSK thin film as deposited on the ZnO single crystal (SC-ZnO/PVSK). This PVSK layer also has a pinhole-free surface and small grain size, like the ITO/PVSK film in Figure 2a, demonstrating that the smooth surface of the ZnO single crystal is not disruptive to the PVSK thin film structure. Figure 2c is a cross-sectional SEM image of the MS-ZnO/PVSK sample, and highlights that while there is good contact between the two materials, the PVSK film has discontinuities arising from the roughness of the ZnO layer (Figure S2, Supporting Information). Figure 2d shows that contact between PVSK and NS-ZnO is not as optimal due to the high surface roughness of the ZnO layer, and while the PVSK infiltrates the nanowires to

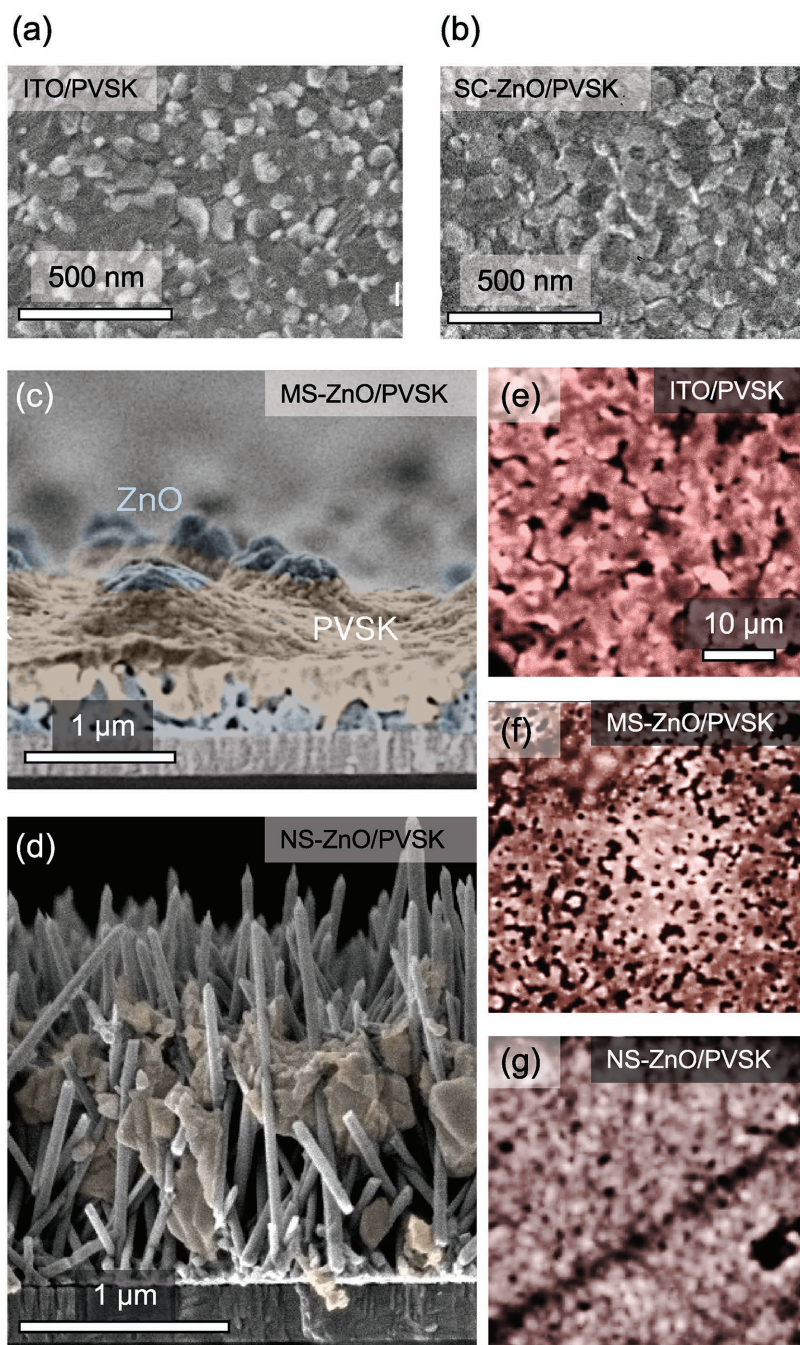


**Figure 2.** a,b) Top-down SEM images of  $\text{CH}_3\text{NH}_3\text{PbI}_3$  films deposited on ITO and SC-ZnO showing very similar morphology. c,d) Side view of  $\text{CH}_3\text{NH}_3\text{PbI}_3$  deposition on MS-ZnO and NS-ZnO. e–g) Fluorescence images of ITO/PVSK, MS-ZnO/PVSK, and NS-ZnO/PVSK show increasingly smaller grain formation with reduction in size of ZnO features. Hence, grain size is now below the microscope resolution limit, which prevents acquisition of a clearer image. Scale bar in (e) applies to (f, g).

form a heterostructure with multiple points of contact between the two materials, coalescing of PVSK occurs in regions deep in the nanostructured layer (Figure S2, Supporting Information). Fluorescence microscope images of three samples, ITO/PVSK, MS-ZnO/PVSK, and NS-ZnO/PVSK, prepared with  $\text{CH}_3\text{NH}_3\text{PbI}_{3-x}\text{Cl}_x$ , are shown in Figure 2e–g, respectively.

These images underline the impact of roughness of the ZnO layers on the PVSK thin film. In Figure 2e, the ITO/PVSK thin film shows a characteristic pattern of large grains of varying fluorescence intensity<sup>[32]</sup> delineated by dark grain boundaries, the latter known to act as recombination centers. A similar image of MS-ZnO/PVSK in Figure 2f shows a decrease in grain size, and a further proliferation of grain boundaries accompanied by even greater reduction in grain size is observed in the fluorescence image of NS-ZnO/PVSK in Figure 2g, reaching the limit of the microscope resolution. These would suggest that ZnO layers with higher surface roughness are detrimental to charge transfer across the device interface<sup>[32,33]</sup> and this conjecture is validated in Figure 3, where we observe increased PVSK PL, instead of PL quenching, the typical signature of efficient ETLs.<sup>[34]</sup>

The PL spectrum of SC-ZnO/PVSK in Figure 3a shows the emission intensity quenching by a factor of  $\approx 3$  when compared to that of ITO/PVSK and is accompanied by a small decrease in room-temperature recombination lifetime (Figure 3b), from 4.9 to 4 ns. The behavior of the PVSK thin films deposited on the micro- and nanostructured ZnO layers is very different. The PL spectra of MS-ZnO/PVSK and NS-ZnO/PVSK are plotted in Figure 3c. MS-ZnO/PVSK exhibits an enhancement of PVSK luminescence by a factor of 20, while PL intensity upsurges by almost  $\times 10^3$  in NS-ZnO/PVSK. Room-temperature time-resolved PL in Figure 3d, and the extracted lifetimes averaged over different spots on the samples summarized in the inset to Figure 3b show that, in conjunction with PL increase, both MS-ZnO/PVSK and NS-ZnO/PVSK heterostructures reduce the recombination lifetimes, by 16% and 55%, respectively. PVSK PL quenching is characteristic of charge extraction from the PVSK layer to the underlying ETL<sup>[34]</sup> (Figure S3, Supporting Information), and together with the reduced lifetime, suggests that SC-ZnO is indeed acting as one. The PL enhancement in Figure 3c, particularly that observed in the NS-ZnO/PVSK, is more reminiscent of Purcell effect, a result supported by the rapid recombination occurring in those samples. The proliferation of grain boundaries in the PVSK thin film when deposited on the micro and nanostructured

ZnO layers might be causing increased confinement of excitons in the smaller PVSK grains, resulting in increased spontaneous emission and faster recombination based on a random walk model.<sup>[35]</sup> The PL enhancement factor in the NS-ZnO/PVSK samples can be driven as high as  $3 \times 10^4$  with excitation power, as shown in the inset to Figure 3d, before it saturates. While this

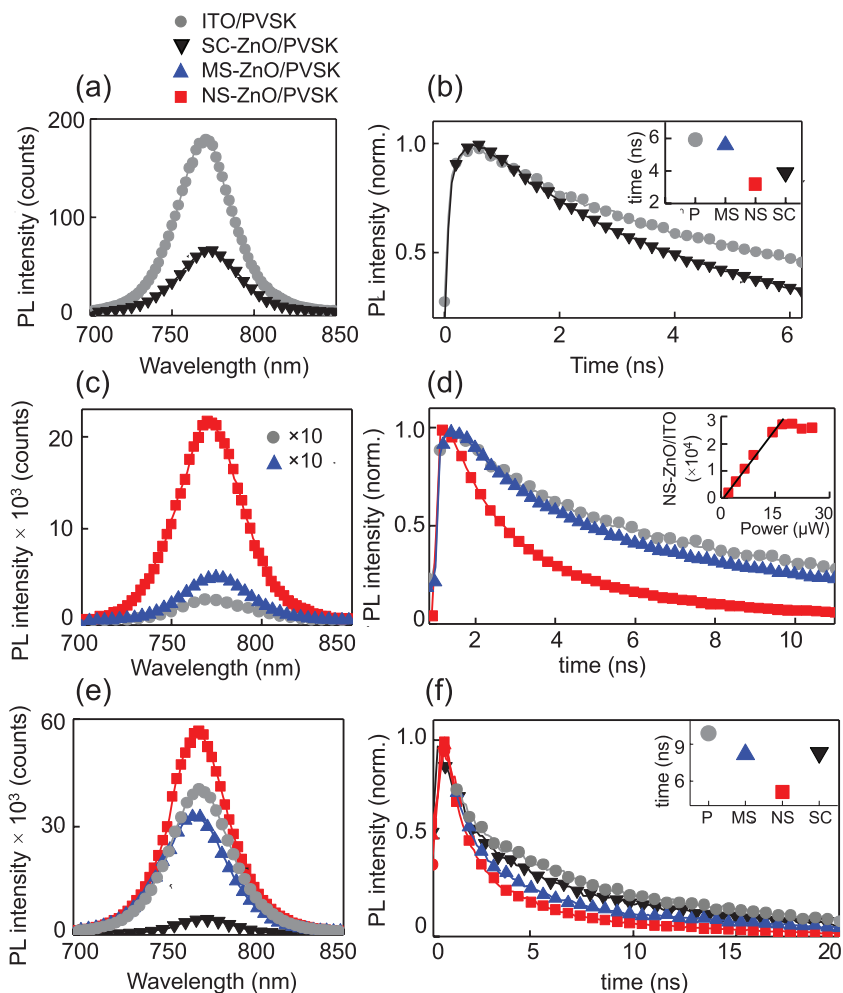


**Figure 3.** a,b) Static and time-resolved PL emission of  $\text{CH}_3\text{NH}_3\text{PbI}_3$  on ITO and SC-ZnO exhibit PL quenching and faster charge extraction in the latter. c,d) Static and dynamic PL comparing results of ITO/PVSK, MS-ZnO/PVSK, and NS-ZnO/PVSK. (b, inset) Average recombination times of  $\text{CH}_3\text{NH}_3\text{PbI}_3$  on the four different ZnO layers. (d, inset) Integrated PL from NS-ZnO/PVSK varying with excitation power, normalized to ITO/PVSK emission. e,f) Static and dynamic PL of  $\text{CH}_3\text{NH}_3\text{PbI}_{3-x}\text{Cl}_x$  deposited on the four layers. (f, inset) Average lifetimes.

combination is not suitable for charge extraction, it demonstrates great potential for optoelectronic applications, such as photodetectors with the capability of magnifying the input signal manyfold. This variation in how PVSK PL is modulated by the ZnO substrates might have a contribution beyond the morphology, since there is an inherent variation in the carrier concentration of the three substrates, resultant of the synthesis process. The single-crystal carrier density<sup>[36,37]</sup> is in the range  $10^{14}$ – $10^{15}$   $\text{cm}^{-3}$ , while that of the MS-ZnO and NS-ZnO is higher,<sup>[38,39]</sup> in the range  $10^{17}$ – $10^{18}$   $\text{cm}^{-3}$ . It is possible that a higher carrier concentration makes MS-ZnO and NS-ZnO substrates inefficient as ETLs, but that cannot be established beyond doubt. It is quite certain, however, carrier density is not the cause of the increased PL emission of the NS-ZnO/PVSK heterostructures, since the MS-ZnO/PVSK does not demonstrate an enhancement anywhere close despite having a similar carrier concentration.

The variation in PVSK characteristics with the use of different halide precursors is well-documented,<sup>[40]</sup> and for

consistency, we repeated our measurements with samples fabricated with lead chloride as the source in the precursor to confirm the trends observed in samples prepared with lead acetate. For  $\text{CH}_3\text{NH}_3\text{PbI}_{3-x}\text{Cl}_x$  thin films annealed in the vacuum oven, the observed trends for PL quenching and exciton recombination lifetime agree with the trends demonstrated with  $\text{CH}_3\text{NH}_3\text{PbI}_3$  thin films. PL intensity of PVSK is reduced by 90% when PVSK is deposited on SC-ZnO, as shown in Figure 3e. Also, as before, PL intensity is enhanced (albeit very slightly, by a factor of 1.4) when NS-ZnO is used. Figure 3f plots the time-resolved PL of  $\text{CH}_3\text{NH}_3\text{PbI}_{3-x}\text{Cl}_x$  on the different ZnO layers, all of which reduce the average recombination lifetime, summarized in the inset. Again, while SC-ZnO and MS-ZnO reduce the average lifetime by  $\approx 20\%$ , use of NS-ZnO results in a lifetime 40% shorter. These results are attributed to similar phenomena as discussed previously: SC-ZnO is effectively extracting electrons from the PVSK layer, whereas NS-ZnO is confining excitons within grains, as indicated by the short lifetime but enhanced PL intensity. However, the phenomenon is not as prominent as in the case of lead acetate based PVSK due to the larger PVSK grains when fabricated with lead chloride precursor.

We have also investigated the properties of thermally annealed  $\text{CH}_3\text{NH}_3\text{PbI}_{3-x}\text{Cl}_x$  thin films, performed using a hot plate at a significantly higher temperature than vacuum annealing ( $110^\circ\text{C}$ ), and over a period thrice as long. High-temperature thermal annealing of PVSK has been associated with reduced number of pores in the film, but also with increased pore size, which results in reduced coverage of the substrate.<sup>[41,42]</sup> Furthermore, annealing for long time periods has been

observed to lead to PVSK decomposition due to the formation of  $\text{PbI}_2$ .<sup>[43,44]</sup> Expectedly, these samples show significantly modified properties. The PVSK thin film deposited on ITO glass appears to be optically almost “dark,” and PL is progressively enhanced by the nanostructured, single-crystalline, and microstructured ZnO layers (Figure S4a, Supporting Information), in that order. Further, incorporation of ZnO prolongs the recombination lifetime for all the samples, indicating electron transfer is hindered for these samples (Figure S4b, Supporting Information). These results underline the importance of the annealing method during fabrication, not only for the quality of the PVSK layer but also for proper interpretation of the electron extraction afforded by ZnO.

### 2.3. Temperature Dependence of PL Tuning

In hybrid PVSK thin films, PL emission has contributions from recombination of both excitons and free electron–hole pairs,

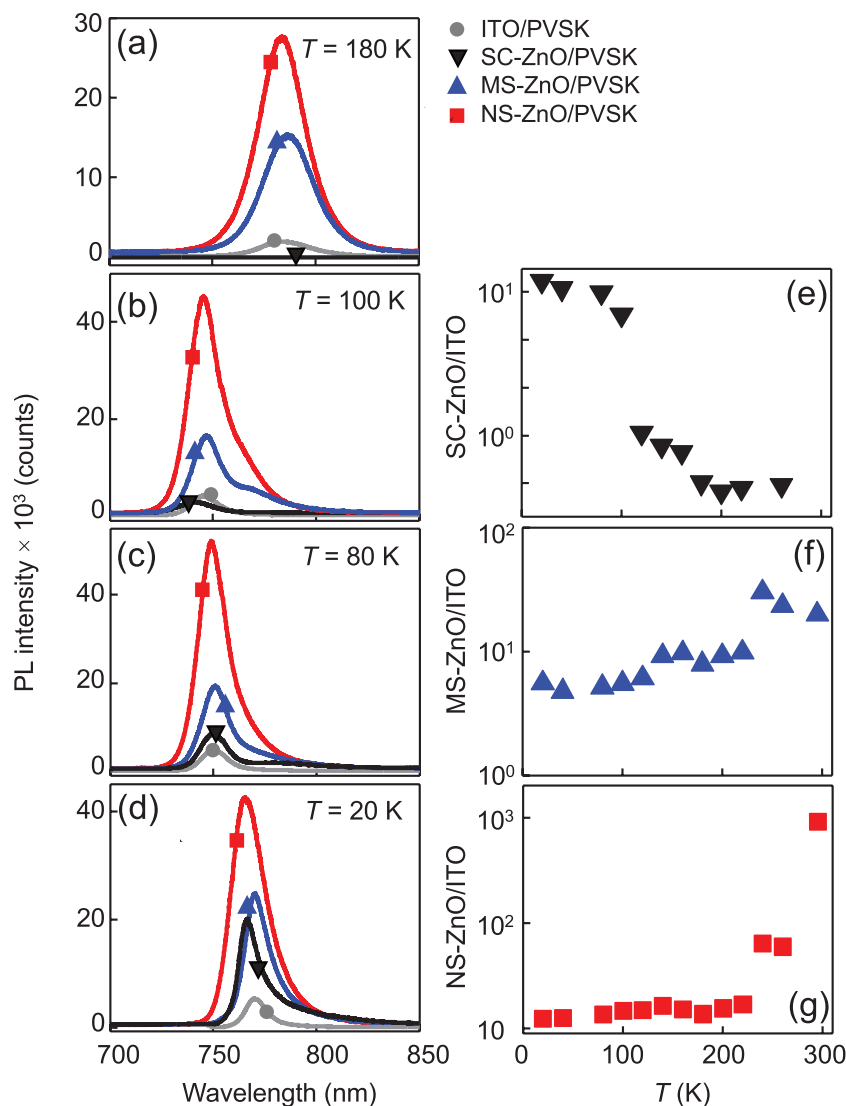


**Figure 4.** a–d) PL spectra of  $\text{CH}_3\text{NH}_3\text{PbI}_3$  deposited on the four different ZnO layers at 180, 100, 80, and 20 K. e–g) The integrated PL intensity of PVSK deposited on SC-ZnO, MS-ZnO, and NS-ZnO, normalized with respect to emission from PVSK on ITO.

with the proportion of each determined by the temperature and the exciton binding energy  $E_B$ . Tuning  $E_B$  has been successfully leveraged to improve interactions at the interface, including charge extraction efficiency and PL enhancement. Some examples comprise the use of heterostructures<sup>[45]</sup> and plasmonic nanoparticles<sup>[46]</sup> to modify  $E_B$  and improve electronic transport properties in hybrid PVSK solar cells. Beyond PVSKs, the use of coulomb engineering through modification of the local dielectric environment<sup>[47]</sup> has been demonstrated to tune  $E_B$  in 2D  $\text{WS}_2$  and  $\text{WSe}_2$  heterojunctions. Integration with a wide bandgap ETL has the potential of tuning  $E_B$  in PVSKs as well, and we investigate that possibility next. **Figure 4** follows the variation in  $\text{CH}_3\text{NH}_3\text{PbI}_3$  emission on the ZnO layers at different temperatures. The spectral shift between the results in **Figure 4a,b** is driven by the structural phase transition. The other notable difference is that while at 180 K PL intensities from all four sample types have the same relationship with respect to the ITO/PVSK

film, from 100 K down, SC-ZnO/PVSK PL is no longer quenched. In fact, by 20 K, SC-ZnO enhances PVSK PL by almost a factor of 4. This variation as a function of temperature  $T$  is shown in **Figure 4e** in the form of the ratio of PL intensities of SC-ZnO/PVSK and ITO/PVSK. Similar data for MS-ZnO/PVSK and ITO/PVSK in **Figure 4f** demonstrate a mild increase in PL over the entire temperature range, without any quenching. Nanostructured ZnO layers affect the PVSK PL most strikingly, affecting a steady enhancement that reaches a thousand-fold by room temperature, in **Figure 4g**. To investigate if the quenching/enhancement driven by the substrates relate to the PVSK thin films, we focus next on calculating the proportion of free and bound charge carriers and if the presence of the different substrates has any noticeable effect.

#### 2.4. Exciton Recombination in PVSK Tuned by ZnO Layers

The variation of spectrally integrated PL intensity with excitation power at different temperatures has proven insightful in estimating the exciton binding energy  $E_B$ . Equation (1) shows the variation of the integrated intensity  $I_{\text{PL}}$  as

$$I_{\text{PL}} \sim Ax^2 [N_{\text{tot}}]^2 + B(1-x)N_{\text{tot}} \quad (1)$$

where  $x$  is the fraction of free charge carriers, and  $(1-x)$  the fraction of excitons that recombine radiatively;  $A$  and  $B$  are the bimolecular and the monomolecular recombination coefficients, respectively.  $N_{\text{tot}}$  is the total charge carrier density, directly proportional to the excitation power  $P$ , implying  $I_{\text{PL}} \propto P^2$  for free charge carriers and  $I_{\text{PL}} \propto P$  for excitonic recombination. Therefore, by fitting a second-

order polynomial to the power-dependent PL of PVSK at any fixed temperature  $T$  (**Figure S5**, Supporting Information), the quadratic and linear coefficients corresponding to free charge carriers and excitons<sup>[25,44]</sup> at that  $T$  can be extracted, which in turn allow  $E_B$  and the relative proportion of free and bound charge carriers to be evaluated, as summarized in **Figure 5**. We use a formalism<sup>[44]</sup> based on the Saha–Langmuir equation shown in Equation (2)

$$\frac{x^2}{1-x} = \frac{1}{N_{\text{tot}}} \left( \frac{2\pi\mu k_B T}{h^2} \right)^{3/2} e^{-E_B/k_B T} \quad (2)$$

$\mu$  is the reduced exciton mass ( $\approx 0.1m_e$ ), where  $m_e$  is the free electron mass,  $k_B$  is the Boltzmann constant, and  $h$  is the Planck's constant. To extract  $E_B$  from the acquired data while accounting for the coefficients  $A$  and  $B$  of Equation (1), we fit Equation (2) to the ratio of the quadratic-to-linear weights versus  $1/T$  (**Figure S6**, Supporting Information).

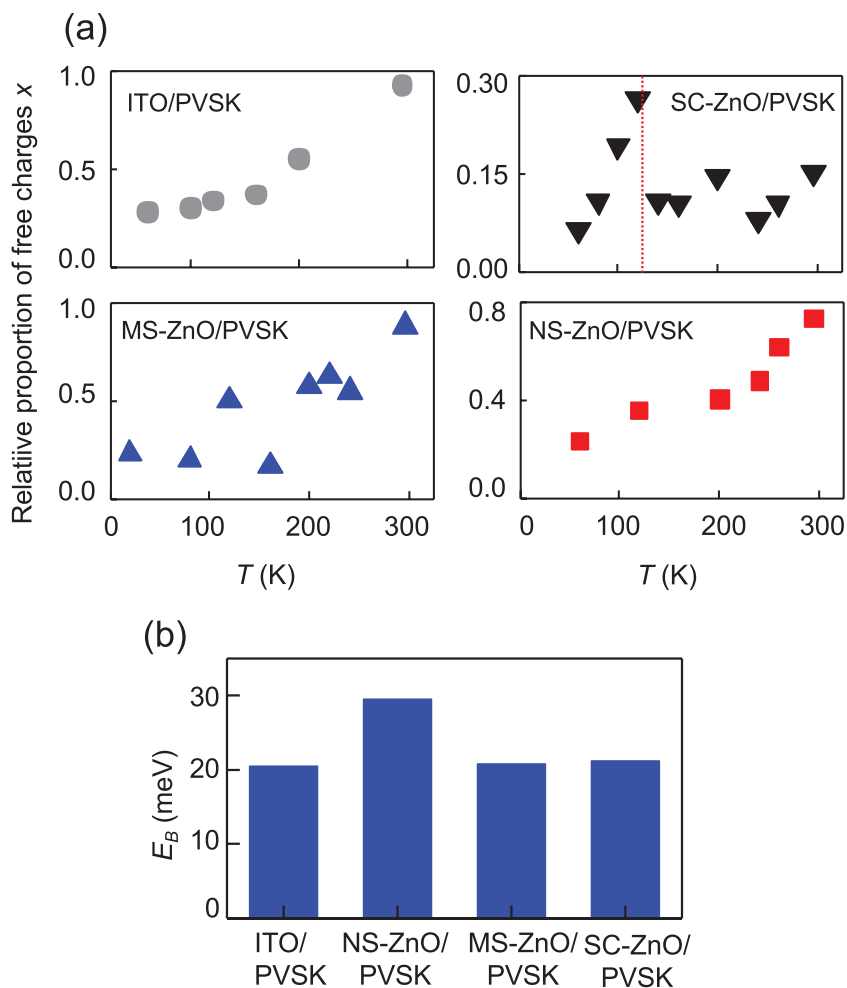


**Figure 5.** a) Relative proportion of free charge carriers varying with temperature  $T$  for  $\text{CH}_3\text{NH}_3\text{PbI}_3$  deposited on ITO and the three ZnO substrates, normalized to the ITO/PVSK result. b) Exciton binding energy  $E_B$  calculated for each type of substrate.

The proportional weights of free charge carriers, normalized to the ITO/PVSK control sample's, are plotted in Figure 5a as functions of  $T$ , while  $E_B$  values for each sample are plotted in Figure 5b. In ITO/PVSK, the proportion of free carriers contributing to recombination decreases with temperature  $T$ , which is typical, as excitonic recombination begins to dominate with reduced  $T$ . The same is the case for the other samples as well, although in SC-ZnO/PVSK there is a nonmonotonicity, with a discontinuity arising around the temperature where the structural phase transition occurs. We have calculated  $E_B$  averaged over the entire temperature range over which PL is collected, but in some instances,<sup>[44]</sup>  $E_B$  has shown different values in the two structural phases, with a smaller binding energy in the low  $T$  orthorhombic phase. This might explain the increase in free carriers around the transition. Aside from this, Figure 5a further shows significantly fewer free charge carriers in SC-ZnO/PVSK at 295 K (70% fewer than in ITO/PVSK), which cannot be attributed to higher  $E_B$ , which is practically unchanged from  $E_B$  in ITO/PVSK, as Figure 5b demonstrates. Therefore, the apparent reduced proportion of free carriers can only be a consequence of transfer from PVSK to SC-ZnO, confirming carrier extraction

indicated by quenching of PL. Additionally, the temperature where free carrier fractional value shows a jump in Figure 5a, indicated by the dashed line, is very close to where PVSK PL is no longer quenched by the SC-ZnO substrate in Figure 4e. MS-ZnO/PVSK behaves most like ITO/PVSK, with  $E_B$  and free carrier proportions both being very similar. Given that these microstructured substrates do not affect PL significantly in Figure 4f, this is not unexpected.

The results from samples incorporating the NS-ZnO substrates are subtler. The free carrier contribution in Figure 5a is 20% less compared to ITO/PVSK, but PL enhancement, rather than quenching, over the entire experimental temperature range affirms that there is no carrier extraction.  $E_B$  is higher than all the other three samples in Figure 5b, and this accounts for fewer free electrons and holes. The question then is: what the underlying cause for the increased binding energy is, and if the same can also account for the markedly reduced recombination time seen in Figure 3d. The surface topology of the NS-ZnO layer most definitely has a role to play, and we have observed the increased roughness disrupts the formation of the PVSK thin films during annealing (Figure S7, Supporting Information). This leads to the formation of smaller grains, with average size on the order of the diffraction limit of the optical microscope in Figure 2g. We speculate that these sub-micrometer sized grains could be confining the excitons, not only limiting charge carrier transport within the PVSK film, but also increasing  $E_B$ . Further, this confinement would account for higher recombination rates, almost like a Purcell effect in optical cavities. Interestingly, in the  $\text{CH}_3\text{NH}_3\text{PbI}_{3-x}\text{Cl}_x$  films with prolonged thermal annealing that results in smaller grains, we observe a similar PL enhancement for all the ZnO substrates, likely arising from the same cause as highlighted here.

### 3. Conclusion

Hybrid perovskites have properties that make them highly desirable for a range of applications, extending well beyond photovoltaics. Customizing them for optimal performance in different applications will necessarily require careful design of device architecture, which makes tailoring interface properties to achieve desired optoelectronic characteristics essential. Based on our work, planar interfaces appear to be the most optimum structure for charge extraction. This result is supported by means of optical measurements which have been used to quantify exciton lifetime, nature of charge carriers recombining to result in PL, and PL intensity quenching. The experimental data are supplemented by calculations of  $E_B$  to better understand

the fundamental processes occurring at the SC-ZnO/PVSK interface. And, while optical measurements portray a clear picture, future endeavors must also include electrical measurements to fully quantify electron flow within the device.

The more interesting part of our findings is the PL enhancement observed in the roughened layers, most significantly in the nanostructured films, which we establish cannot be attributed to the carrier density of the ZnO substrates. Instead of reducing  $E_B$  and increasing charge carrier extraction as might have been expected owing to the increased contact area between the ZnO and PVSK, we observed enhanced exciton binding by carrier confinement and up to several thousand-fold increase in PVSK emission intensity. This is an aspect of charge modulation in hybrid PVSK thin films that have not been focused on, centered on optoelectronic properties rather than photovoltaics. Hybrid PVSKs are renowned for excellence in the former as well, with consistently high quantum yield and long charge lifetimes. Our results highlight the possibility of entirely novel applications that would exploit these characteristics, paving the way for device platforms that have not been considered in the realm of PVSKs yet.

#### 4. Experimental Section

ZnO nanowires (NS-ZnO) are synthesized using previously reported techniques.<sup>[23]</sup> A catalyst containing solution was prepared using poly(4-vinyl pyridine) (P4VP, Polymer Source, Inc.) of molecular weight  $60\,000\text{ g mol}^{-1}$  and Zn(II) acetylacetonate (Sigma Aldrich) dissolved in 1-butanol (Sigma Aldrich). The P4VP weight ratio is 0.3 wt% and the metal-to-polymer molar ratio is 0.8:1. The solution was mixed for 5 h under magnetic stirring and was deposited on indium tin oxide (ITO) glass substrate by spin-coating at 3000 rpm for 30 s. After the deposition of each layer the sample was baked for 2 min at 100 °C to remove the solvent and prevent intermixing. The samples were then annealed at 350 °C for 30 min in air to remove the polymer template and form nanoparticles. Although the annealing temperature might reduce the conductivity of the ITO layer, it does not influence the interaction between the PVSK and ZnO layers. Nanowires were grown using a solution-based hydrothermal technique in a Teflon-lined stainless steel autoclave, with the active side of the substrates facing down.  $20 \times 10^{-3}\text{ M}$  of hexamethylenetetramine (HMTA, VWR, 99+%) and zinc nitrate hexahydrate (VWR, 99.998%) mixed in deionized water were used for the growth.<sup>[23]</sup> The synthesis was done at 95 °C in an oven (Yamato ADP 21 vacuum oven) for 6 h. Once nanowire synthesis was complete the nanowires underwent post-annealing at 400 °C in air.

Electrodeposition of microstructured ZnO (MS-ZnO) was achieved using conditions reported elsewhere.<sup>[24]</sup> Electrodeposition was done in a three-electrode cell maintained at 88 °C with the aid of an oil bath, with zinc foil as the counter electrode and Ag/AgCl as the reference electrode, raised above the solution to keep at lower temperature. A Princeton Instruments galvanometer was used to monitor and provide the necessary voltage for deposition. Deposition was conducted using deionized water based solutions of  $5 \times 10^{-3}\text{ M}$  of  $\text{ZnCl}_2$  (Alfa Aesar) and 0.1 M KCl (VWR). The solution was saturated with molecular oxygen and slight  $\text{O}_2$  bubbling was kept throughout the deposition. The applied potential is  $-0.82\text{ V}$  versus Ag/AgCl and deposition was finished when the total electrical charge exchanged was  $1.1\text{ C cm}^{-2}$ . A ZnO single crystal, commercially purchased from Tokyo Denpa Inc., was used as the lowest surface roughness sample.

PVSK ( $\text{CH}_3\text{NH}_3\text{PbI}_3$ ) precursor was prepared from 2.64 M of methylammonium iodide (MAI, Luminescence Technology Corp.) and 0.88 M of lead (II) acetate trihydrate (Sigma Aldrich), dispersed in N,N-dimethylformamide (DMF). PVSK thin films were spin-coated on UV/ozone-treated ITO glass substrate or UV/ozone-treated ZnO at

4000 rpm for 30 s and were subsequently annealed on a hot plate at 100 °C for 5 min, in a nitrogen environment. Similarly, for preparation of  $\text{CH}_3\text{NH}_3\text{PbI}_{3-x}\text{Cl}_x$  thin films, 2.64 M of MAI and 0.88 M of lead chloride (Sigma Aldrich) were dispersed in DMF, followed by spin-coating at 4000 rpm for 30 s. Annealing of samples was done using two different methods: on a hot plate in  $\text{N}_2$  environment at 110 °C until the surface turned dark brown or in a vacuum oven at 60 °C until samples turned dark brown.<sup>[39,48]</sup>

A pulsed Ti:sapphire laser (Mira, Coherent Inc., repetition rate 13 ns) was frequency-doubled using a BBO crystal to 355 nm for the optical measurements of ZnO, and tuned to 408 nm for acquiring PVSK PL. An Acton 300i spectrometer with a thermoelectrically cooled charge-coupled device, with spectral resolution of 0.18 nm, was used to collect PL spectra. Temperature-dependent measurements were conducted in a cryo-free system from Advanced Research Systems (base temperature 10 K). A time-correlated single photon counting (TCSPC) system from Picoquant was used for time-resolved PL. An Agilent UV-vis spectrophotometer was used to record the absorbance spectra of the samples and SEM images were obtained with Zeiss Gemini SEM 500. Fluorescence images of the PVSK thin films were obtained using a confocal microscope (Zeiss LSM 700) which allows the possibility of dual-mode fluorescence-SEM imaging.

#### Supporting Information

Supporting Information is available from the Wiley Online Library or from the author.

#### Acknowledgements

This work was supported by NASA MIRO Grant No. NNX15AQ01A. K.N. and S.S. acknowledge support of the Southern California Edison Graduate Fellowships. Part of imaging characterizations in this work was performed under User Proposals (No. 3715) at the Molecular Foundry, Lawrence Berkeley National Lab, supported by the Office of Basic Energy Sciences, of the U.S. Department of Energy under Contract No. DE-AC02-05CH11231.

#### Conflict of Interest

The authors declare no conflict of interest.

#### Keywords

carrier extraction, exciton binding energy, hybrid perovskite, nanostructures, zinc oxide

Received: February 7, 2018

Revised: March 22, 2018

Published online:

- [1] A. Kojima, K. Teshima, Y. Shirai, T. Miyasaka, *J. Am. Chem. Soc.* **2009**, *131*, 6050.
- [2] M. Saliba, T. Matsui, J. Y. Seo, K. Domanski, J. P. Correa-Baena, M. K. Nazeeruddin, S. K. Zakeeruddin, W. Tress, A. Abate, A. Hagfeldt, M. Grätzel, *Energy Environ. Sci.* **2016**, *9*, 1989.
- [3] N. J. Jeon, J. H. Noh, W. S. Yang, Y. C. Kim, S. Ryu, J. Seo, S. I. Seok, *Nature* **2015**, *517*, 476.
- [4] NREL, Solar Cell Efficiency Chart 2018, <http://www.nrel.gov/pv/> (accessed: January 2018).

- [5] Q. Chen, N. De Marco, Y. Yang, T. B. Song, C. C. Chen, H. Zhao, Z. Hong, H. Zhou, Y. Yang, *Nano Today* **2015**, *10*, 355.
- [6] S. D. Stranks, G. E. Eperon, G. Grancini, C. Menelaou, M. J. Alcocer, T. Leijtens, L. M. Herz, A. Petrozza, H. J. Snaith, *Science* **2013**, *342*, 341.
- [7] B. Susrutha, L. Giribabu, S. P. Singh, *Chem. Commun.* **2015**, *51*, 14696.
- [8] Z. K. Tan, R. S. Moghaddam, M. L. Lai, P. Docampo, R. Higler, F. Deschler, M. Price, A. Sadhanala, L. M. Pazos, D. Credgington, F. Hanusch, T. Bein, H. J. Snaith, R. H. Friend, *Nat. Nanotechnol.* **2014**, *9*, 687.
- [9] M. Liu, M. B. Johnston, H. J. Snaith, *Nature* **2013**, *501*, 395.
- [10] X. Yin, P. Chen, M. Que, Y. Xing, W. Que, C. Hiu, J. Shao, *ACS Nano* **2016**, *10*, 3630.
- [11] H. Zhu, Y. Fu, F. Meng, X. Wu, Z. Gong, Q. Ding, M. V. Gustafsson, M. T. Trinh, S. Jin, X.-Y. Zhu, *Nat. Mater.* **2015**, *14*, 636.
- [12] D. Li, G. Dong, W. Li, L. Wang, *Sci. Rep.* **2015**, *5*, 7902.
- [13] G. Yang, H. Tao, P. Qin, W. Ke, G. Fang, *J. Mater. Chem. A* **2016**, *4*, 3970.
- [14] M. M. Lee, J. Teuscher, T. Miyasaka, T. N. Murakami, H. J. Snaith, *Science* **2012**, *338*, 643.
- [15] P. Qin, A. L. Domanski, A. K. Chandiran, R. Berger, H. J. Butt, M. I. Dar, T. Moehl, N. Tetreault, P. Gao, S. Ahmad, M. K. Nazeeruddin, M. Grätzel, *Nanoscale* **2014**, *6*, 1508.
- [16] Y. Zhao, K. Zhu, *J. Phys. Chem. Lett.* **2013**, *4*, 2880.
- [17] S. S. Kim, S. Bae, W. H. Jo, *Chem. Commun.* **2015**, *51*, 17413.
- [18] D. Liu, T. L. Kelly, *Nat. Photonics* **2014**, *8*, 133.
- [19] D. Y. Son, J. H. Im, H. S. Kim, N. G. Park, *J. Phys. Chem. C* **2014**, *118*, 16567.
- [20] J. You, L. Meng, T. B. Song, T. F. Guo, Y. Yang, W. H. Chang, Z. Hong, H. Chen, H. Zhou, Q. Chen, Y. Liu, N. De Marco, Y. Yang, *Nat. Nanotechnol.* **2016**, *11*, 75.
- [21] H. Zhou, Q. Chen, G. Li, S. Luo, T. Song, H.-S. Duan, Z. Hong, J. You, Y. Liu, Y. Yang, *Science* **2014**, *345*, 542.
- [22] K. Mahmood, B. S. Swain, A. R. Kirmani, A. Amassian, *J. Mater. Chem. A* **2015**, *3*, 9051.
- [23] Y. Liu, J. F. Flores, J. Q. Lu, *J. Phys. Chem. C* **2014**, *118*, 19387.
- [24] T. Pauporté, E. Jouanno, F. Pellé, B. Viana, P. Aschehoug, *J. Phys. Chem. C* **2009**, *113*, 10422.
- [25] M. Saba, M. Cadelano, D. Marongiu, F. Chen, V. Sarritzu, N. Sestu, C. Figus, M. Aresti, R. Piras, A. G. Lehmann, C. Cannas, A. Musinu, F. Quochi, A. Mura, G. Bongiovanni, *Nat. Commun.* **2014**, *5*, 5049.
- [26] P. Docampo, J. M. Ball, M. Darwich, G. E. Eperon, H. J. Snaith, *Nat. Commun.* **2013**, *4*, 2761.
- [27] P. Yang, H. Yan, S. Mao, R. Russo, J. Johnson, R. Saykally, N. Morris, J. Pham, R. He, H.-J. Choi, *Adv. Funct. Mater.* **2002**, *12*, 323.
- [28] H. Li, C. Liang, K. Zhong, M. Liu, G. A. Hope, Y. Tong, P. Liu, *Nanoscale Res. Lett.* **2009**, *4*, 1183.
- [29] R. Elilarrasi, G. Chandrasekaran, *Mater. Chem. Phys.* **2010**, *121*, 378.
- [30] S. Dhara, P. K. Giri, *Nanoscale Res. Lett.* **2011**, *6*, 504.
- [31] W. Zhang, M. Saliba, D. T. Moore, S. K. Pathak, M. T. Hörantner, T. Stergiopoulos, S. D. Stranks, G. E. Eperon, J. A. Alexander-Webber, A. Abate, A. Sadhanala, S. Yao, Y. Chen, R. H. Friend, L. A. Estroff, U. Wiesner, H. J. Snaith, *Nat. Commun.* **2015**, *6*, 6142.
- [32] D. W. deQuilettes, S. M. Vorpahl, S. D. Stranks, H. Nagaoka, G. E. Eperon, M. E. Ziffer, H. J. Snaith, D. S. Ginger, *Science* **2015**, *348*, 683.
- [33] W. Nie, H. Tsai, R. Asadpour, J.-C. Blancon, A. J. Neukirch, G. Gupta, J. J. Crochet, M. Chhowalla, S. Tretiak, M. A. Alam, H.-L. Wang, A. D. Mohite, *Science* **2015**, *347*, 522.
- [34] C. Liu, K. Wang, P. Du, C. Yi, T. Meng, X. Gong, *Adv. Energy Mater.* **2015**, *5*, 1402024.
- [35] J.-H. Im, J. Luo, M. Franckevius, N. Pellet, P. Gao, T. Moehl, S. M. Zakeeruddin, M. K. Nazeeruddin, M. Grätzel, N.-G. Park, *Nano Lett.* **2015**, *15*, 2120.
- [36] M. Suscavage, M. Harris, D. Bliss, P. Yip, S.-Q. Wang, D. Schwal, L. Bouthilllette, J. Bailey, M. Callahan, D. C. Reynolds, R. L. Jones, C. W. Litton, *MRS Internet J. Nitride Semicond. Res.* **1999**, *4S1*, G3.40.
- [37] G. Juárez-Díaz, J. Martínez, M. L. García-Cruz, R. Peña-Sierra, J. A. García, M. Pacio, *Phys. Status Solidi C* **2010**, *7*, 957.
- [38] I. Mora-Seró, F. Fabregat-Santiago, B. Denier, J. Bisquert, R. Tena-Zaera, J. Elias, C. Lévy-Clément, *Appl. Phys. Lett.* **2006**, *89*, 203117.
- [39] X. Yang, A. Wolcott, G. Wang, A. Sobo, R. C. Fitzmorris, F. Qian, J. Z. Zhang, Y. Li, *Nano Lett.* **2009**, *9*, 2331.
- [40] K. Nikolaidou, S. Sarang, C. Hoffman, B. Mendewala, H. Ishihara, J. Q. Lu, B. Ilan, V. Tung, S. Ghosh, *Adv. Opt. Mater.* **2016**, *4*, 2126.
- [41] G. E. Eperon, V. M. Burlakov, P. Docampo, A. Goriely, H. J. Snaith, *Adv. Funct. Mater.* **2014**, *24*, 151.
- [42] A. Dualeh, N. Tetreault, T. Moehl, P. Gao, M. K. Nazeeruddin, M. Grätzel, *Adv. Funct. Mater.* **2014**, *24*, 3250.
- [43] F. X. Xie, D. Zhang, H. Su, X. Ren, K. S. Wong, M. Grätzel, W. C. H. Choy, *ACS Nano* **2015**, *9*, 639.
- [44] S. Sarang, H. Ishihara, Y.-C. Chen, O. Lin, A. Gopinathan, V. C. Tung, S. Ghosh, *Phys. Chem. Chem. Phys.* **2016**, *18*, 28428.
- [45] O. Voznyy, B. R. Sutherland, A. H. Ip, D. Zhitomirsky, E. H. Sargent, *Nat. Rev. Mater.* **2017**, *2*, 17026.
- [46] W. Zhang, M. Saliba, S. D. Stranks, Y. Sun, X. Shi, U. Wiesner, H. J. Snaith, *Nano Lett.* **2013**, *13*, 4505.
- [47] A. Raja, A. Chaves, J. Yu, G. Arefe, H. M. Hill, A. F. Rigosi, T. C. Berkelbach, P. Nagler, C. Schuller, T. Korn, C. Nuckolls, J. Hone, L. E. Brus, T. F. Heinz, D. R. Reichman, A. Chernikov, *Nat. Commun.* **2017**, *8*, 15251.
- [48] H. Ishihara, W. Chen, Y.-C. Chen, S. Sarang, N. De Marco, O. Lin, S. Ghosh, V. Tung, *Adv. Mater. Interfaces* **2016**, *3*, 1500762.